nature communications

Article

https://doi.org/10.1038/s41467-026-71389-w

# Solution-processed photovoltaic and thermoelectric hybrid systems with efficiency exceeding 50%

Received: 6 April 2025

Accepted: 23 March 2026

Published online: 03 April 2026

Check for updates

Zhanzhao Yin[1,2,4], Ding Zhang[3,4], Longyu Li[1,2], Yuping Gao[1,2], Yongsheng Liu[1,2], Xiangjian Wan[1,2], Rujun Ma[3] ✉ & Yongsheng Chen[1,2] ✉

Photovoltaic-thermoelectric (PV-TE) hybrid systems offer a platform for enhancing the energy conversion efficiency of photovoltaic devices. However, they still suffer from energy losses and limited efficiency improvements owing to underutilized parasitic thermal energy and electrical parameters mismatches between PV and TE components. Here, we presented a comprehensive theoretical analysis and simulation based on a PV-TE Thermo-Electrical Coupling Model, predicting that the maximum efficiency of the system could reach 60.34% with state-of-the-art PV and commercial TE technologies. Following this model, we fabricated hybrid systems with organic and perovskite solar cells coupled with thermoelectric cells, achieving record-high efficiencies of 34.85% and 42.03% at 298 K, and 43.16% and 50.28% at 313 K, respectively, under AM 1.5 G illumination, with optimal thermal utilization and current matching between series-connected PV and TE modules. This work highlights the potential of PV-TE hybrid systems and could offer guidance for designing higher-efficiency systems, driving future advancements in photovoltaics.

Sunlight, as a clean and sustainable energy, has long been harnessed through photovoltaic technology on a global scale to generate electricity. Recently, significant advancements have sparked renewed excitement in the field. Notable progress has been made recently in areas such as organic solar cells (OSCs)[1,2] and perovskite solar cells (PSCs)[3,4], as well as in thermophotovoltaics (TPV)[5,6] and concentrating photovoltaics (CPV)[7,8]. TPV and CPV technologies have garnered considerable interest due to their relatively high efficiencies[5,9]. However, they require ultrahigh-temperature heat sources[10] and condensers[11], which complicates their structural design.

As emerging photovoltaic technologies, solution-processed solar cells such as OSCs and PSCs are catching more interest due to their many unique advantages, such as simple fabrication process, low cost, lightweight, and potential for roll-to-roll large-area production[4,12,13]. To date, the best power conversion efficiency achieved for single-junction OSCs and PSCs and silicon-based solar cells has risen to 21%[2,14,15], 27%[4,16,17], and 28%[18], respectively. However, further efficiency improvement remains challenging, as these cells can only utilize a limited portion of sunlight in the visible and near-infrared regions, and also the parasitic heat, mainly generated from the sub-bandgap photons and thermalization loss, has been wasted[19,20]. For any photovoltaic technology, following the law of conservation of energy, to achieve the maximum electricity output, the sunlight must be used in the maximum manner and the parasitic heat generated in the process should be minimized or used at the maximum[21,22].

Meanwhile, as it is well-known, the heat generated during the operation of solar cells, primarily from infrared sunlight[21,23] and the parasitic heat[19,20], not only reduces the efficiency (Supplementary Fig. 1) but also impacts their operational lifespan. This issue is particularly critical for emerging OSCs and PSCs technologies. Therefore,

[1]State Key Laboratory of Elemento-Organic Chemistry, Frontiers Science Center for New Organic Matter, Nankai University, Tianjin, China. [2]Key Laboratory of Functional Polymer Materials, Institute of Polymer Chemistry, College of Chemistry, Nankai University, Tianjin, China. [3]School of Materials Science and Engineering, Nankai University, Tianjin, China. [4]These authors contributed equally: Zhanzhao Yin, Ding Zhang. ✉e-mail: malab@nankai.edu.cn; yschen99@nankai.edu.cn

converting the parasitic heat from solar cells into electricity, while maintaining a low operating temperature, could not only enhance the utilization of solar energy and boost power conversion efficiency but also extend the lifespan of the solar cells[22,24].

Thermoelectric (TE) technology, which can directly convert thermal energy into electricity via Seebeck effect[25,26], has been long used for parasitic heat recovery and utilization in many scenarios[27–29]. Thus, it would be a perfect fit to combine PV and TE cells together[21,22]. Indeed, since the concept of PV-TE hybrid system was first proposed in the 1970s[30], many pioneering theoretical simulations and experimental studies have been carried out[22,31–33]. But surprisingly, a comprehensive investigation of the literatures finds that, up to date, the best reported simulated efficiency is only 33.8% for PV-TE hybrid systems[9,34]. Regarding the experimental studies, unfortunately, the highest reported efficiency of PV-TE hybrid systems is merely approximately 23% under AM 1.5 G solar illumination[32,35]. These surprisingly low efficiencies in literatures for PV-TE hybrid systems in terms of both theoretical and experimental studies indicate that there must be some fundamental issues, and thus some serious and comprehensive analysis is warranted. It should be noted that the prevailing efficiency measurement for PV-TE hybrid systems is typically defined as the ratio of electrical energy output to incident solar energy input, which is consistent with the calculation of the power conversion efficiency (PCE) for standalone PV cells[21,22,35]. Contributions from ambient thermal energy or additional cooling sources are typically not considered. This method enables a direct comparison of the performance improvement of PV-TE hybrid systems relative to standalone PV cells.

Above the obvious requirement that the PV and TE cells themselves should be state-of-the-art in the PV-TE hybrid systems, it is crucial that the parasitic heat generated from the sunlight must be efficiently converted into electricity through the TE module to maximize overall system efficiency[36–38]. Moreover, the output power (efficiency) of any PV-TE hybrid system must adhere to basic physics principles for multi-cell systems to achieve the maximum or energy lossless coupling output[39,40]. Clearly, the possible maximum output power of the PV-TE hybrid system is the sum of the two given individual PV and TE cells/modules according to the energy conservation law, and this requires the two modules of PV and TE in the hybrid system to have electrically matchable characteristic parameters (note the PV and TE cells are very different in their electrical parameters)[41–43]. Therefore, to achieve the best-performed PV-TE hybrid system, it is essential to optimize the overall configuration of the hybrid system to simultaneously maximize parasitic heat utilization and achieve energy lossless coupling output between the PV and TE submodules. Considering the overwhelming complexity, systematic modeling is first required. Thus, we constructed a PV-TE Thermo-Electrical Coupling Model (PT-TECM) to analyze the conditions of maximizing heat utilization and matching electrical parameters, and then simulated the efficiency of PV-TE hybrid systems through the COMSOL Multiphysics® platform.

Following the proposed model above, we predicted that the maximum efficiency of the optimized PV-TE hybrid system could reach 60.34% by using the best single-junction PSCs[4,16,17] and commercialized TE materials[26,44,45]. Guided by these simulations, our fabricated optimized solution-processed solar cells (OSCs and PSCs) and thermoelectric hybrid systems connected in series achieved record efficiency of 34.85% / 43.16% and 42.03% / 50.28% at environmental temperatures ($T_{atm}$) of 298 K/313 K (with the active area of 0.24/0.28 $cm^2$) under AM 1.5 G solar illumination, respectively. To demonstrate scalability, we further fabricated a larger-area 1.0 $cm^2$ OSC-TE hybrid system using the same strategy. This larger system also exhibited a high efficiency of 33.48% at 298 K, with an efficiency similar to that of the small-area OSC-TE hybrid system. Furthermore, we fabricated a large-area, flexible and wearable OSC-TE hybrid system capable of directly powering a sensor for real-time pulse monitoring, while the individual OSC module could not achieve this due to its relatively low output power. We believe the results of both theoretical modeling and experimental results demonstrated in this work would provide valuable design guidelines for high-performance PV-TE hybrid systems, particularly for solution-processed PV cells, and significantly expand their application potential in various fields.

## Results and discussions

### Theoretical analysis and modeling for optimized utilization of thermal energy and electrical parameter matching

As mentioned above, to address the overwhelming complexity and guide the fabrication and optimization of such high-performed hybrid systems, the PT-TECM was established (Supplementary Notes 1 and 2) to achieve both the conditions for optimal parasitic heat utilization and electrical parameter matching and further simulate the efficiency ($\eta$) of the PV-TE hybrid systems. The simulation involved the development of heat transfer and equivalent circuit models using the COMSOL Multiphysics® platform (Supplementary Note 2). For efficient harvesting of parasitic thermal energy, TE cells are configured as a stacked module located beneath the PV module in the PV-TE hybrid system (Supplementary Note 1.1). In terms of electrical parameter matching, the maximum output power of the hybrid system can be achieved either by connecting two different types of batteries in parallel or in series (Supplementary Note 1.2). However, as detailed in Supplementary Note 1.3, due to the changing temperature and light intensity of the actual application environment, the voltage and current of both PV and TE cells (modules) vary correspondingly. This would lead to severe charging/discharging between the PV and TE cells if connected in parallel, even leading to overheating or battery damage. But for the system connected in series, the PV and TE cells (modules) can still operate relatively stable. Therefore, the connection of PV and TE modules in series would be the best choice and was thus used in this study. For a series-connected PV-TE hybrid system, current matching must be achieved to maximize output power. This means that the PV and TE modules must produce the same output current at their respective maximum output power points to ensure the highest efficiency of the entire system.

Guided by the theoretical analysis above, a heat transfer model of stacked TE modules was used to optimize thermal energy utilization (Supplementary Note 2.1). Current matching between the PV and TE modules was achieved through the appropriate series and parallel configuration of their respective sub-modules, and then the efficiency of the PV-TE hybrid system was calculated using an equivalent circuit model (Supplementary Note 2.2). Importantly, without maximizing parasitic heat utilization and electrical matching, the series-connected OSC or PSC and TE hybrid systems showed a very limited efficiency improvement of ~2–3% (Supplementary Fig. 2), similar to previous reports[21,24]. Using the PT-TECM, it is possible to simulate and optimize the output power and efficiency of any combination of PV and TE cells with different types, and the simulated results subsequently were used to guide us to carry out relevant experiments. Figure 1a illustrates the structure of the PV-TE hybrid system used in both simulations and experiments, where the PV (OSC or PSC) module (top) is connected to the TE module (bottom) in series with a thermal conductive layer between them, and the effective area of the PV and TE modules keeps always the same. Figure 1b shows the detailed structure of the OSC, PSC, and TE cell units used in this study. The TE cells are made of bismuth telluride ($Bi_2Te_3$)-based thermoelectric materials, due to their high thermoelectric performance and stability at room temperature[46,47]. The equivalent electrical circuits for the PV-TE hybrid systems are shown in Fig. 1c. AFM images of the OSC and PSC films reveal smooth surface topography. GIWAXS analysis of the OSC indicates well-defined molecular packing and orientation, while XRD patterns of the PSC confirm the formation of a well-crystallized perovskite phase (Supplementary Figs. 3, 4). UV-vis absorption spectra

demonstrate the spectral complementarity between the PV and TE components for efficient solar energy harvesting (Supplementary Fig. 5). These characterizations demonstrate the reproducibility of device fabrication and provide a solid physical foundation for the integration of the PV-TE hybrid system.

### Simulations and experiments for optimized thermal energy utilization

To optimize the utilization of parasitic thermal energy generated by solar cells, a heat transfer model of the stacked PV-TE hybrid structure was established (Supplementary Note 2.1). Using this model, the thermoelectric temperature difference ($\Delta T$) and voltage ($V_{TE}$) can be obtained by solving Equations S3-S8 (Supplementary Note 2.1). The established general heat transfer framework was then applied to a specific OSC-TE hybrid configuration, consisting of a single OSC (with a reported efficiency of 18% in our previous work[48]) and multiple commercial TE cells (see Supplementary Note 2.1 and Supplementary Fig. 6 for details). Both the OSC and each individual TE cell possess an identical active area of 0.04 $cm^2$.

To find the best conditions for heat utilization, the $\Delta T$ with different numbers ($k$) of TE layers in the system was simulated using the model, where $k \in [1, 10]$ (Supplementary Fig. 7). The hot-side temperature of the PV-TE hybrid system is determined by the heat generated from the solar cell under AM 1.5 G solar illumination, while the cold-side temperature could be controlled by various cooling methods. To achieve a large temperature difference and evaluate the maximum efficiency of the hybrid system, the cold-side temperature of the system was maintained at 0 °C (273 K). In the likely practical applications scenarios, without external energy input, the condition (0 °C) might be achieved when the PV-TE hybrid system is deployed in marine environments with seawater cooling (from the equator to the poles, seawater temperature decreases gradually from ~ 25 °C to ~ 0 °C or even below 0 °C), as well as in polar regions or space, as detailed in the final applications section.

Detailed simulation results for $\Delta T$ and $V_{TE}$ of the 0.04 $cm^2$ OSC-TE hybrid systems with different numbers of TE layers are shown in Fig. 2a (the blue shaded area) and Supplementary Fig. 8. In this case, since the overall performance of the series-connected hybrid system is mainly determined by $\Delta T$ and $V_{TE}$ from the TE module[22], the relationship between the $V_{TE}$ and the number of TE layers ($k$) were selected to evaluate the efficiency of hybrid system. The shaded region in Fig. 2a represents the performance fluctuation range of the system due to changes in the temperature of the surrounding air, which exchanges heat convectively with the system (Supplementary Note 3). As the $k$ increases from 1 to 10, the $\Delta T$ and $V_{TE}$ gradually increase and reach approximately constant when $k$ exceeds 6. Then, the efficiency of the OSC-TE hybrid system was obtained by inserting the $V_{TE}$ into the equivalent circuit model and solving Equations S9-S13 (Supplementary Note 2.2). As a result, the OSC-TE hybrid system reaches the maximum efficiency improvement ($\Delta\eta = \eta_{OSC\text{-}TE} - \eta_{OSC}$) at $k = 6$ (the red shaded area in Fig. 2a), compared to the individual OSC.

Guided by the simulation results above, we fabricated a series of PV-TE hybrid systems using the OSCs with a reported efficiency of 18% in our previous work[48] and commercial TE cells with measured total Seebeck coefficient of 9.72 mV/K (Supplementary Fig. 6). The bottom temperature of the PV-TE hybrid system was maintained at 273 K. The experiment results of $\Delta T$, $V_{TE}$, and $\Delta\eta$ of the system with different values of $k$ are shown in Fig. 2a and Supplementary Fig. 9a.

Note the overall performance enhancement ($\Delta\eta$) of the series-connected hybrid system is mainly determined by $\Delta T$ and $V_{TE}$ from the TE module. At $k = 6$, the $\Delta T$ and $V_{TE}$ reach their maximum value (approximately 28 K and 0.28 V, respectively), indicating that the TE module achieves optimal thermal energy utilization. At this condition, the 0.04 $cm^2$ OSC-TE hybrid system achieved its highest efficiency of 23.99% (Supplementary Fig. 9b), corresponding to the $\Delta\eta$ of 6.17%. Thus, we can conclude that the PV-TE hybrid system could maximize thermal energy utilization at $k = 6$. The consistency between the experimental and simulation results demonstrates the accuracy of our model and the reliability of the experimental data, highlighting the potential of our PT-TECM for performance optimization.

### Simulations and experiments for current matching

Besides maximizing thermal energy utilization, current matching between the PV and TE modules is also a must for achieving maximum efficiency. Note the current at the maximum output power point of the TE module ($k = 6$) was approximately 7.0 mA, significantly larger than the current of the 0.04 $cm^2$ OSC (1.0 mA). Therefore, to achieve the current matching, the PV module must be constructed with $n$ solar cells connected in parallel to increase its current (Supplementary Fig. 10). Meanwhile, the areas of the PV and TE modules must be kept the same. Thus, each layer of the TE submodule was built with $m$ TE cells connected in series, and then each layer of the TE submodule is again connected in series to form the final TE module, maintaining a constant current in the TE module. The effective area of the PV and TE modules must be equal to ensure maximum utilization of parasitic heat, therefore $n = m$. The corresponding heat transfer model and equivalent circuit model for current matching are shown in Supplementary Notes 2.1 and 2.2. We can obtain the *J-V* curve and efficiency of the PV-TE hybrid system with different areas (corresponding to $n = m \in [1, 9]$, $k = 6$) by solving the Equations S9-S13 in Supplementary Note 2.2. The simulated results of $\Delta\eta$ of the entire hybrid systems with different electrical matching are presented in the shaded area of Fig. 2b. Again, the shaded region reflected the performance fluctuation of the system due to changes in the temperature of the surrounding air, which exchanges heat convectively with the system (Supplementary Note 4). Note the $\Delta\eta$ first increases and then decreases gradually. The PV and TE modules achieved electrical matching (the same current) and thus the highest simulated system efficiency when $n = m = 6$, $k = 6$.

Guided by these simulation results, corresponding experiments were conducted using the OSCs and TE cells mentioned above. To achieve the best and also reliable experimental results, we prepared various OSC parallel modules with effective areas ranging from 0.04 to 0.36 $cm^2$, corresponding to $n \in [1, 9]$, to have a complete and systematic experimental evaluation. As indicated by the above results and discussion on heat utilization, the number of TE layers was fixed at 6 ($k = 6$) to maximize heat utilization. Infrared thermal imaging of the PV-TE hybrid systems illustrates the thermal energy harvesting and the cooling effect provided by the TE modules, highlighting the thermal synergy between the PV and TE components (Supplementary Fig. 11). The experimental current ratio between OSC and TE modules and $\Delta\eta$ of the OSC-TE hybrid system with different areas were shown in Fig. 2b. As the system area increases ($n = m \in [1, 9]$, $k = 6$), the measured current ratio of the OSC and TE modules increased from 0.13 to 1.49, with $\Delta\eta$ initially increasing and then decreasing, peaking when the current ratio reached 1.0 (Fig. 2b and Supplementary Fig. 12a). At the peak point, the 0.24 $cm^2$ OSC-TE hybrid system ($n = m = 6$, $k = 6$) achieved the maximum heat utilization and current matching simultaneously, resulting in the highest $\Delta\eta$ of approximately 16.0% with energy lossless coupling output (Supplementary Fig. 12b), which is consistent with the simulated results (Fig. 2b and Supplementary Note 4). It is noted that the efficiency calculation method of the PV-TE hybrid system (Equation S13, Supplementary Note 2.2) follows the widely used approach in this field[21,22,35], where the efficiency is the ratio of electrical energy output to solar energy input. Thus, $\Delta\eta$ represents the ratio of the electricity generated by the TE module to the input solar energy. Figure 2c shows that the OSC-TE hybrid system ($n = m = 6$, $k = 6$) achieved the maximum efficiency of 34.85% at 298 K under AM 1.5 G solar illumination (Supplementary Table 1), with statistical distribution confirming reproducibility (Supplementary Fig. 13a). Furthermore, the efficiency of the 0.24 $cm^2$ OSC-TE hybrid system with different TE

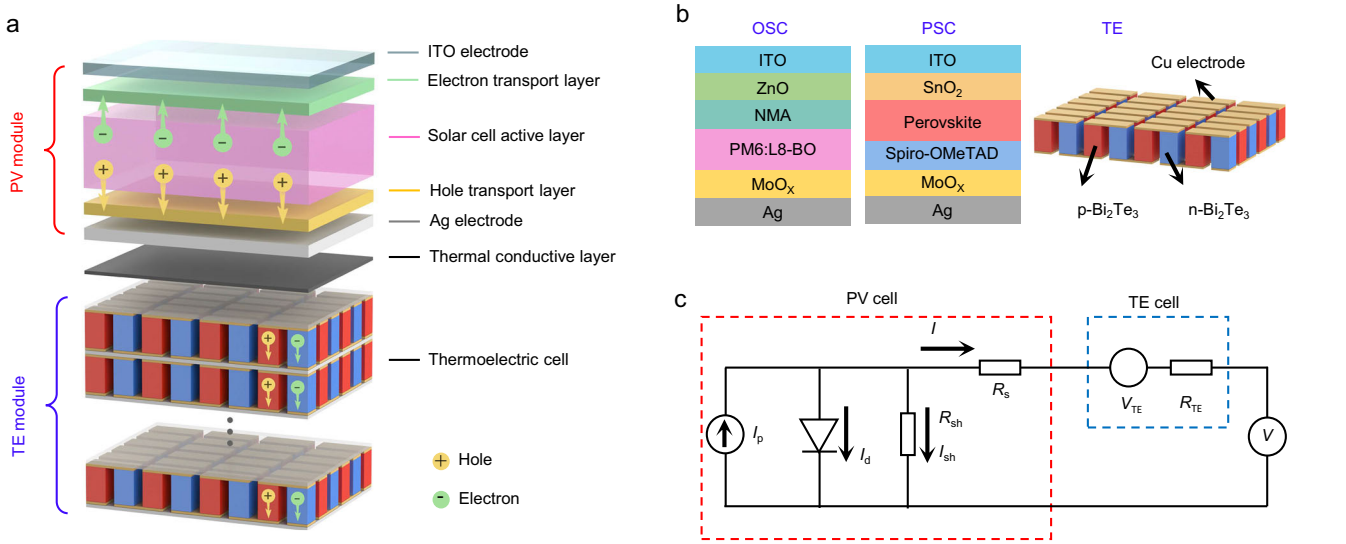


**Fig. 1 | Architecture and working principle of the PV-TE hybrid system.** **a** Schematic illustration of the PV-TE hybrid system. PV and TE modules are connected in series, and all TE cells are connected in series. **b** Architecture of OSC, PSC, and TE cells. For the OSC, the active layer is PM6:L8-BO, with ZnO/NMA and MoOx serving as the electron transport layer and hole transport layer, respectively. In the PSC, the active layer is the perovskite material, while $SnO_2$ and Spiro-OMeTAD/MoOx function as the electron transport layer and hole transport layer, respectively. The TE cell unit consists of multiple p/n $Bi_2Te_3$ legs connected in series, with a copper (Cu) layer serving as electrodes. **c** Equivalent electric circuit of the OSC-TE or PSC-TE hybrid systems. The OSC/PSC is modeled as a single-diode equivalent circuit, which consists of a photocurrent source in parallel with a diode and a shunt resistance ($R_{sh}$), together with a series resistance ($R_s$). The TE cell is modeled as a voltage source ($V_{TE}$) with a series resistance ($R_{TE}$). $I_p$ is the photogenerated current, $I_{sh}$ is the current through the shunt resistance, $I_d$ is the current through the diode, and $I$ is the output current.

layers (keep $n = m = 6$, $k \in [5, 7]$) was also evaluated (Supplementary Fig. 13b), and the experimental results further confirm that $k = 6$ is indeed the optimal value for maximizing thermal energy utilization.

Following the design guideline for optimal OSC-TE hybrid systems, we further fabricated PSC-TE hybrid systems using high-efficiency PSCs (approximately 26% efficiency) reported in our previous work[49]. As shown in Fig. 2d, the 0.24 $cm^2$ PSC-TE hybrid system ($n = m = 6$, $k = 6$) achieved the maximum efficiency of 42.03% at 298 K (Supplementary Table 2), with statistical distribution confirming reproducibility (Supplementary Fig. 14). Under optimal coupling conditions, Figure 2e, f show that the total output power of the integrated PV-TE hybrid system is nearly equal to the sum of the maximum output powers of the PV and TE modules when operating independently. This demonstrates that the system achieved energy lossless coupling between the PV and TE components.

Note that all the above simulated and experimental results of the system are based on basic PV and TE cells with an area of 0.04 $cm^2$. To investigate the scalability of the system, we fabricated a larger-area 1.0 $cm^2$ OSC-TE hybrid system using a single OSC and a six-layer TE module, with both the OSC and TE units having the same area of 1.0 $cm^2$. As shown in Supplementary Fig. 15 and Table 3, the 1.0 $cm^2$ OSC-TE hybrid system also exhibited similar efficiency improvement from 17.13% to 33.48%. The similar efficiency, independent of the device area, would be important for advancing larger-area PV-TE hybrid systems with high efficiency, as the large-area fabrication would be one of the critical factors for practical applications. So far, both the PV (OSC and PSC) and TE devices have achieved large-area module fabrication. A 204 $cm^2$ OSC module with a certified power conversion efficiency of 14.5% was achieved in 2024[50]. The PSC module, with a size of 2 $m^2$, achieved a certified record efficiency of 20.05% in 2025[51]. Bismuth telluride-based thermoelectric generators have also been widely produced and applied at large scale[52]. These results indicate that the PV-TE hybrid system could have excellent potential for scalability and would be capable of large-scale fabrication and application as technology progresses.

Stability would be also one of the critical factors for practical applications. The PV (OSC and PSC) and TE units have demonstrated excellent stability under continuous illumination and temperature fluctuations. For the photostability, to date, the OSC could retain about 93% of their initial efficiency after 2000 hours of continuous maximum power point tracking (MPPT) under 1 sun condition[53]. The PSC could also retain about 82% of their initial efficiency after 2500 h of continuous MPPT under 1 sun condition[54]. For the thermal stability, to date, the OSC could retain 94% of their initial efficiency after 1032 hours of 85 °C/85% relative humidity damp heat and 200 thermal cycles (−40 °C to 85 °C) tests[55]. The PSC could also keep 92% of the initial efficiency when ageing at 85 °C for 1800 h and 94% after 200 thermal cycles between −40 °C and + 85 °C[56]. Furthermore, bismuth telluride-based thermoelectric generators have successfully achieved commercial production and application due to their exceptional stability[52,57].

To assess the stability of the PV-TE hybrid system, we compared the stability of the integrated system with that of each standalone unit under the same testing conditions. The photostability of standalone PV (OSC and PSC) and PV-TE (OSC-TE and PSC-TE) hybrid systems was evaluated under the ISOS-L-1 protocol. The experimental results indicated that both the OSC-TE and PSC-TE hybrid systems exhibited enhanced photostability compared to the standalone OSC and PSC due to the ability of TE module to harvest heat and provide cooling (Supplementary Fig. 16). Thermal stability was assessed under the ISOS-T-2 protocol by subjecting standalone PV (OSC and PSC) and PV-TE (OSC-TE and PSC-TE) hybrid systems to thermal cycles between 25 °C and 65 °C. The OSC and PSC integrated within the hybrid system exhibited similar thermal stability compared to the standalone OSC and PSC after 100 thermal cycles (Supplementary Fig. 17a, b). The TE module exhibited negligible change in output voltage and current after 100 thermal cycles (Supplementary Fig. 17c). In summary, the enhanced photostability and similar thermal stability of PV-TE hybrid system compared with the standalone PV units indicate that the integrated system could achieve or even exceed the reported stability of

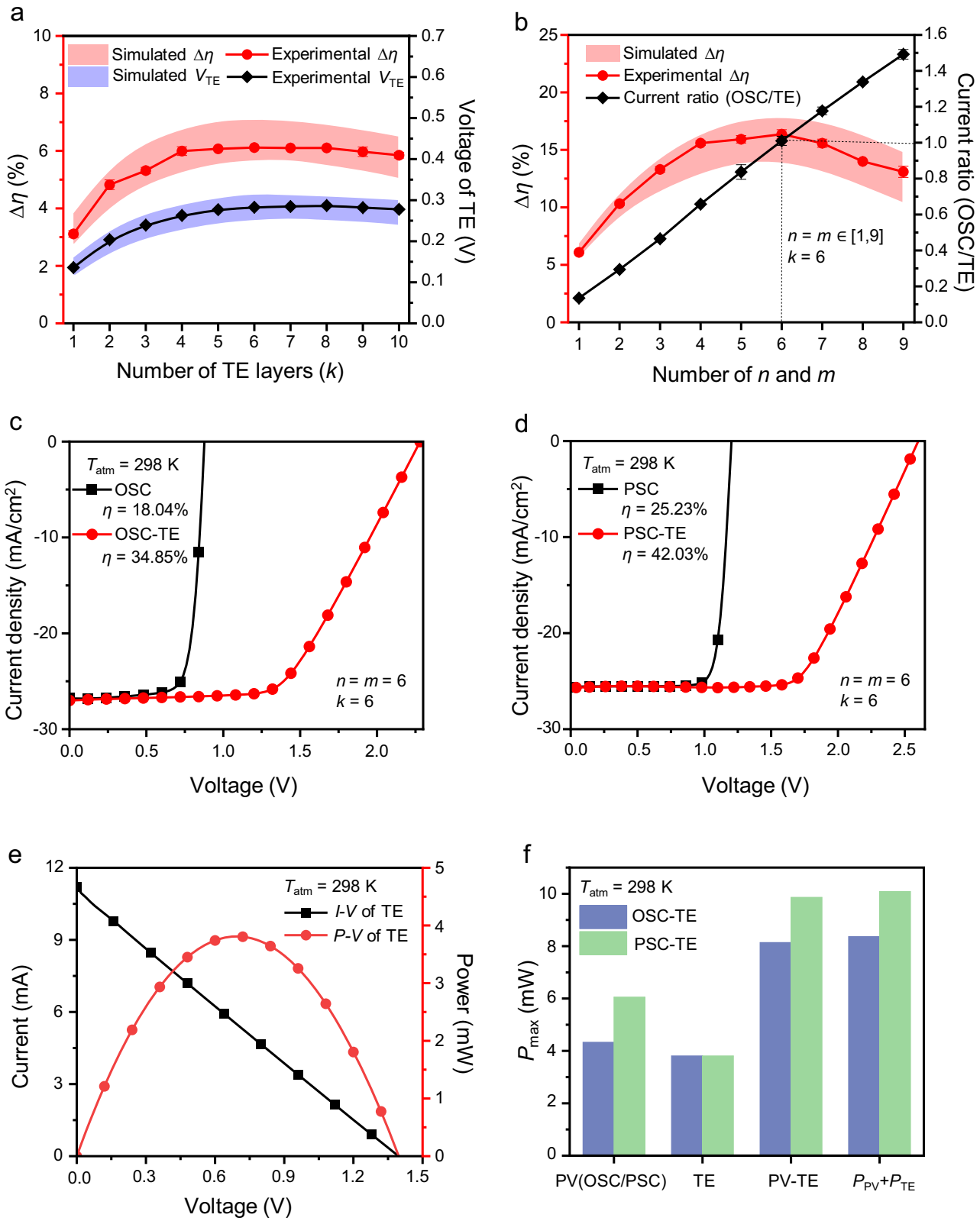


the PV units, demonstrating the system's potential for reliable, long-term practical applications.

### Parametric analysis and record-high efficiencies of PV-TE hybrid systems

To investigate the key factors influencing the efficiency of PV-TE hybrid system, a parametric study was conducted using the PT-TECM. The simulated results indicated that the efficiency of the PV-TE hybrid system increases with higher TE material figure of merit ($zT$) and higher PV cell efficiency (Fig. 3a and Supplementary Note 5). Moreover, a larger $\Delta T$ across the TE module, achieved by a lower cold-side temperature or a higher environmental temperature, can further improve the system efficiency (Fig. 3b and Supplementary Note 6). Additional parameters that might influence system performance, such as the

**Fig. 2 | Optimization of the performance of PV-TE hybrid systems.** **a** Experimental and simulated TE voltage ($V_{TE}$) and performance enhancement ($\Delta\eta$) of 0.04 $cm^2$ OSC-TE hybrid systems with varying numbers of TE layers ($k \in [1, 10]$), compared to the individual OSC. The cold-side temperature was maintained at 273 K. The shaded regions represent the fluctuation range of $V_{TE}$ and $\Delta\eta$ due to the variation in the temperature of the air that conducting convective heat transfer with the systems. **b** The current ratio between OSC and TE modules, and $\Delta\eta$ of OSC-TE hybrid systems relative to the standalone OSC with varying areas of $0.04 \times n$ $cm^2$, where $n \in [1, 9]$. $n$ represents the number of 0.04 $cm^2$ OSC units connected in parallel, and $m$ represents the number of 0.04 $cm^2$ TE units connected in series in each layer. $n$ is equal to $m$ due to the same areas of the PV and TE units, as well as the final module, to optimize heat transfer. The PV or TE current is measured at maximum power points when modules operate independently. The shaded band indicates efficiency fluctuation of the systems, due to the variation in the air temperature conducting convective heat transfer with the systems. In both (**a**, **b**) the center of the error bar is defined as the average value, and error bar is defined as the standard deviation, which is calculated from the statistical results of at least five individual devices. **c**, **d** Experimental champion *J-V* curves of OSC-TE (**c**) and PSC-TE (**d**) hybrid systems ($n = m = 6$, $k = 6$) at 298 K, corresponding to a system area of 0.24 $cm^2$. $T_{atm}$ is the environment temperature and $\eta$ is the power conversion efficiency. **e** *J-V* and *P-V* characteristics of the TE module in the optimized OSC-TE and PSC-TE hybrid systems at 298 K. **f** Power contribution of the PV and TE components in the optimized hybrid systems at 298 K.

convective heat transfer coefficient and thermal interface material properties, are presented in Supplementary Fig. 18.

Therefore, to explore the efficiency limit of the PV-TE hybrid system, we further carried out the simulation using the state-of-the-art PV cells (OSC with ~ 21% efficiency[2,14,15] and PSC with ~27% efficiency[4,16,17]) and the best commercial $Bi_2Te_3$-based TE materials ($zT \approx 1.0$ at room temperature[26,44,45]) (Fig. 3c and Supplementary Note 7). At 298 K (room temperature), the simulated optimal OSC-TE and PSC-TE hybrid systems ($n = m = 6$, $k = 6$) could achieve maximum efficiency of 40.67% and 47.06% under AM 1.5 G solar illumination, respectively. At 313 K (the environment temperature in a typical hot summer), the optimal OSC-TE and PSC-TE hybrid systems ($n = m = 8$, $k = 6$) could reach maximum efficiency of 53.88% and 60.34%, respectively. The reason that $n$ and $m$ are larger at 313 K compared to 298 K is that the higher environment temperature increases the $\Delta T$ and current of the TE module, thereby requiring more PV units connected in parallel for current matching.

To verify the simulated results at 313 K, based on the existing OSC (18% efficiency) [48] and PSC (26% efficiency)[49] in our laboratory, we further measured the efficiency of the OSC-TE and PSC-TE hybrid systems at 313 K. As shown in Fig. 3d, the OSC-TE and PSC-TE hybrid systems ($n = m = 7$, $k = 6$) achieved the maximum efficiency of 43.16% and 50.28% at 313 K under AM 1.5 G solar illumination, respectively (Supplementary Tables 4, 5), with statistical distribution confirming reproducibility (Supplementary Figs. 19, 20). Under optimal coupling conditions, the total output power of the integrated PV-TE hybrid system is also nearly equal to the sum of the maximum output powers of the PV and TE modules when operating independently at 313 K (Supplementary Fig. 21). Compared to the simulation results (Fig. 3c), the lower efficiencies observed in experiments (Fig. 3d) can be attributed to non-ideal practical factors, primarily a lower $zT$ of the employed TE module ($zT \approx 0.9$, compared to $zT \approx 1.0$ in simulation) and the neglect of interfacial thermal resistance in the simulation model. Figure 3e compares the simulated and experimental efficiency of our PV-TE hybrid systems in this work with that of previously reported representative OSC-TE, PSC-TE, and inorganic PV-TE hybrid systems in literatures. Note our optimal OSC-TE and PSC-TE hybrid systems have achieved record-high efficiency of 43.16% and 50.28% at 313 Kunder AM 1.5 G solar illumination, respectively, significantly exceeding the efficiency of previously reported OSC-TE[24,31], PSC-TE[21,22,32,35,58], and inorganic PV-TE[33,40,59,60] hybrid systems in literatures (Supplementary Table 6). Our PV-TE hybrid systems also show great advantages and competitiveness, compared with reported tandem PV devices, PV-TE hybrid systems with radiative cooling, and concentrated PV-TE hybrid systems (Supplementary Table 7). Furthermore, as indicated by the simulation in Fig. 3c, it is expected that with continued advancements in PV and TE technologies, the maximum achievable efficiency of PV-TE hybrid systems should be even better.

## Discussion in application prospect

To explore the application potential of PV-TE hybrid systems, we developed a flexible, large-area OSC-TE hybrid system, and integrated it into wearable clothing (Fig. 4a, Supplementary Figs. 22–24). The integrated system achieved a higher $V_{oc}$, enabling direct operation of a pulse sensor for physiological signal monitoring, whereas the individual OSC could not power the sensor (Fig. 4b, Supplementary Fig. 25). Furthermore, the flexible OSC-TE hybrid system maintained stable performance after 1000 bending cycles, demonstrating its potential as a wearable power source (Supplementary Fig. 26).

Beyond wearable applications in daily life, our PV-TE hybrid systems might hold potential for deployment in some extreme environments. As shown in Fig. 3b, a lower cold-side temperature can increase the $\Delta T$ of the TE-module and thereby improve the efficiency of the PV-TE hybrid system. This prompts us to think about some possible practical scenarios. For instance, seawater serves as a massive constant-temperature source, and Antarctic and Arctic seawater is much cooler in particular. Under solar irradiation, a large $\Delta T$ across the TE module can be achieved when the PV-TE hybrid system floats at the seawater surface, providing a possible ideal application scenario for PV-TE hybrid systems (Fig. 4c). To estimate the power generation potential of the PV-TE hybrid system in marine environments, outdoor performance testing was conducted under sufficient sunlight and wind-free conditions, on one day in June (22 June 2025) and three days in September (7 - 9 September 2025) in Tianjin, China (39.1076° N, 117.1734° E). (Supplementary Fig. 27). The OSC-TE hybrid system achieved maximum average efficiencies of 35.03% in June and 29.16% in September, while the PSC-TE hybrid system reached 40.71% in June and 35.83% in September (Supplementary Fig. 28). The higher efficiency of the hybrid systems in June compared to September was attributed to higher environment temperature in June, which is consistent with our laboratory results (Fig. 3b). The outdoor maximum efficiency of the PV-TE hybrid system experienced an efficiency loss of approximately 9% in June and 14% in September relative to laboratory measurements under ideal steady-state conditions (Fig. 3d).

Additionally, space provides abundant solar and thermal energy, with sunlight unobstructed by the atmosphere, enabling solar cells to operate at high efficiency. When integrated into a satellite, the PV-TE hybrid systems could experience a significant $\Delta T$ between the sunny and dark sides, enabling the TE module to generate substantial extra amounts of electricity (Fig. 4d). Thus, the greater potential demonstrated in this work indicates that PV-TE hybrid systems might be much more competitive than previously thought for many possible applications and even to support human activities in ocean and space environments in the future (Supplementary Note 8).

It is important to note that these scenarios remain conceptual, and real-world deployment will require corrosion-resistant encapsulation, mechanical durability, and long-term validation. Further specific hurdles that must be addressed include the efficiency and stability limitations of OSCs and PSCs, large-area fabrication and integration of PV and TE modules, and performance fluctuations of the PV and TE units in dynamic environments. Cost consideration also remains a potential issue.

Possible strategies to overcome these issues include material design and interfacial engineering[56,61,62], optimizing the fabrication

https://doi.org/10.1038/s41467-026-71389-w

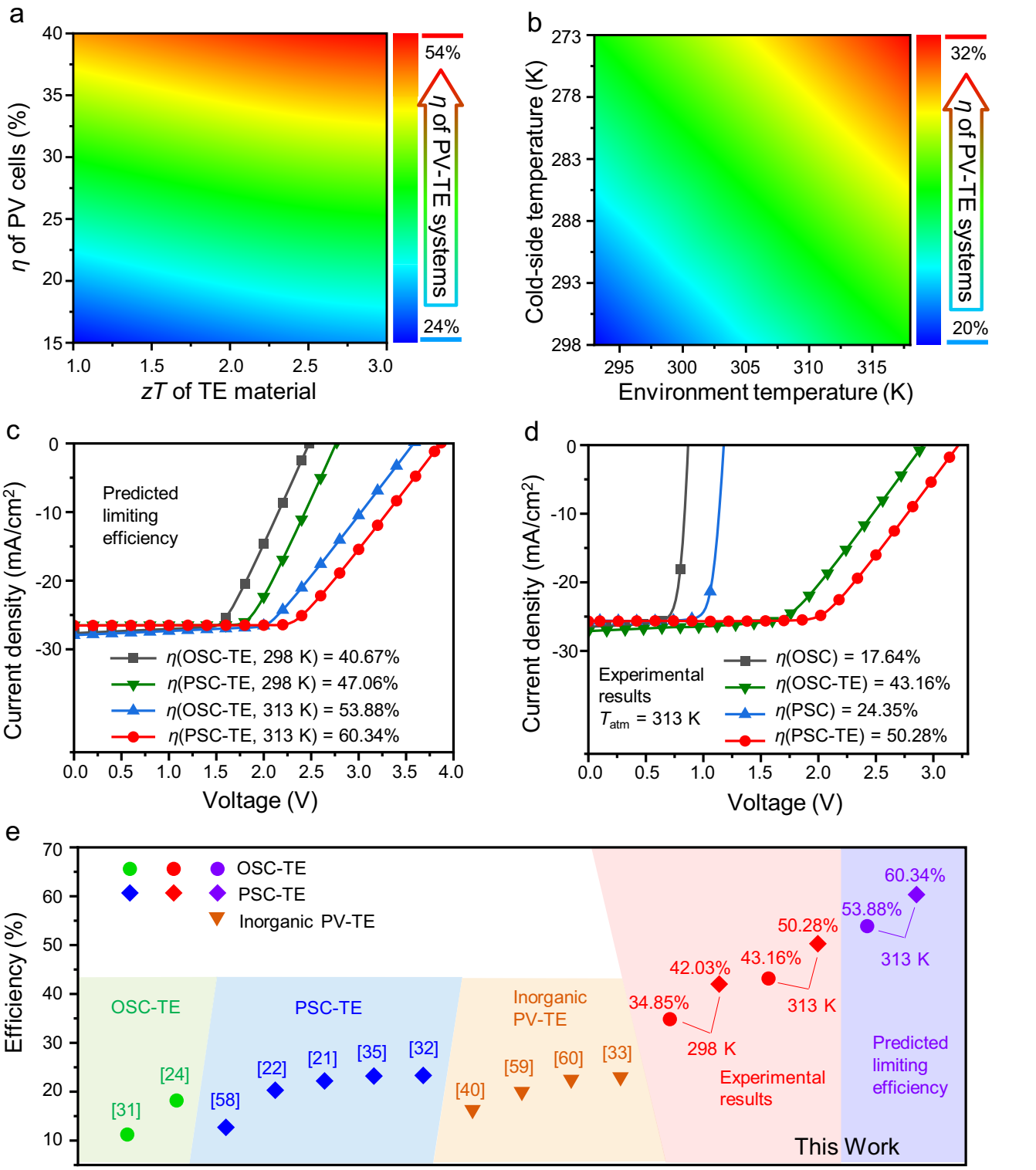


**Fig. 3 | Parametric analysis and efficiency limits. a** Effect of the TE-material figure of merit ($zT$) and efficiency of PV cells on the efficiency of the 0.04 $cm^2$ OSC-TE hybrid system ($n = m = 1$, $k = 6$) at 298 K under AM 1.5 G solar illumination, with a cold-side temperature of 273 K. **b** Effect of cold-side and environmental temperatures on the efficiency of the 0.04 $cm^2$ OSC-TE hybrid system ($n = m = 1$, $k = 6$) under AM 1.5 G solar illumination. The PT-TECM analysis is based on steady-state thermal equilibrium and does not incorporate transient variations in irradiance, wind speed, or ambient temperature. **c** Simulated *J-V* curves of optimized PV-TE hybrid systems at 298 K and 313 K under AM 1.5 G solar illumination, with a cold-side temperature of 273 K, based on the state-of-the-art single-junction OSCs[2,14,15] and PSCs[4,16,17] reported in literatures and the best commercial $Bi_2Te_3$-based TE materials[26,44,45]. **d** Experimental *J-V* curves of 0.28 $cm^2$ PV-TE hybrid systems ($n = m = 7$, $k = 6$) at 313 K under AM 1.5 G solar illumination, with a cold-side temperature of 273 K. Note that these peak efficiencies (e.g., > 50%) are obtained under controlled steady-state conditions, including AM1.5 G solar illumination and a regulated cold-side temperature. For performance deviations under outdoor conditions, see Supplementary Figs. 27 and 28. **e** Comparison of efficiency in this work with representative OSC-TE[24,31], PSC-TE[21,22,32,35,58], Inorganic PV-TE[33,40,59,60] hybrid systems under AM 1.5 G solar illumination reported in literatures.

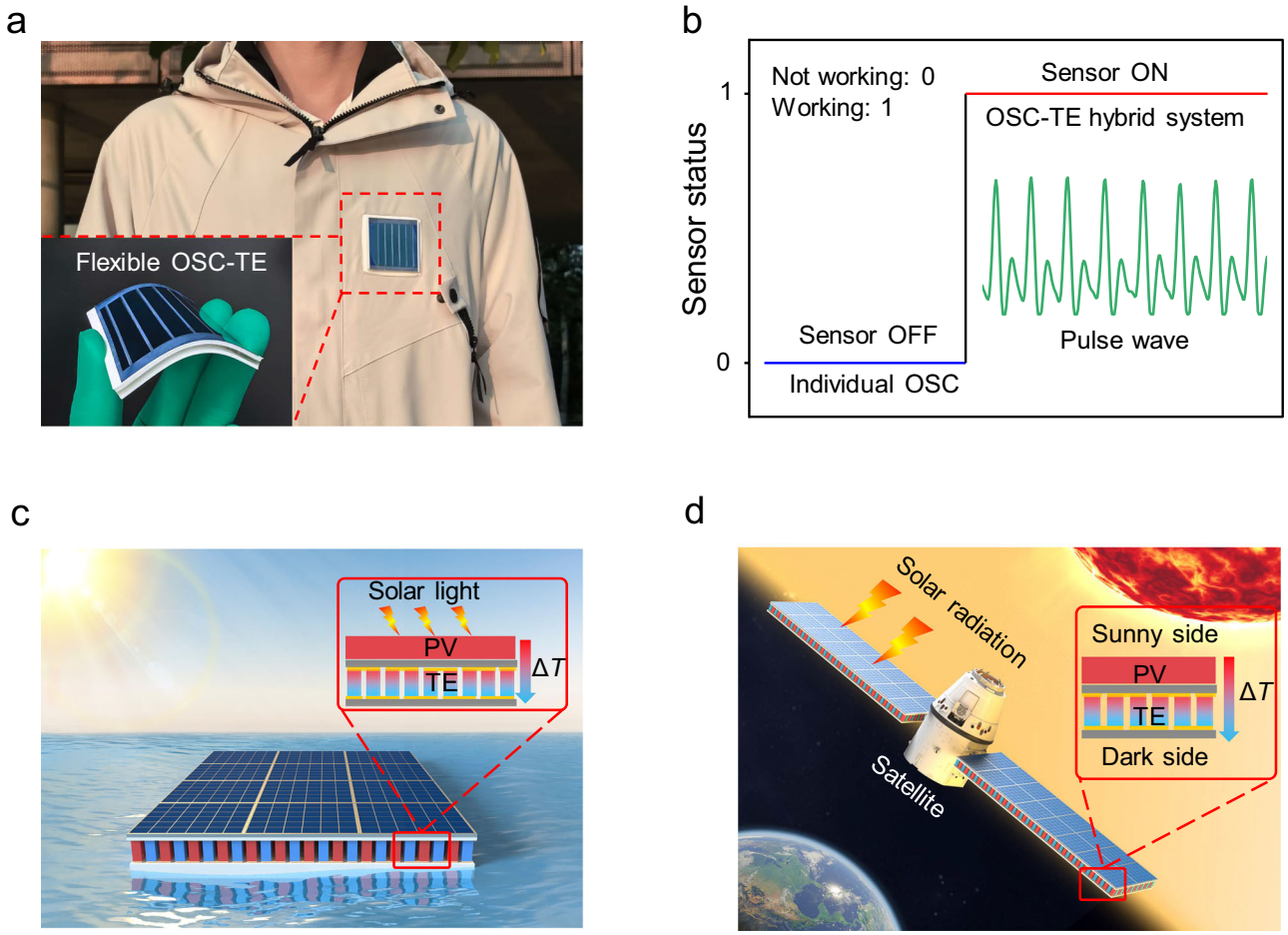


**Fig. 4 | Application prospect of the PV-TE hybrid systems. a** Photograph of the flexible and wearable OSC-TE hybrid system. **b** Demonstration of the OSC-TE hybrid system driving a sensor for real-time pulse monitoring under AM 1.5 G solar illumination, while the individual OSC cannot achieve this. **c**, Potential applications in ocean environments. From the equator to the poles, seawater temperature decreases gradually from ~ 25 °C to ~ 0 °C or even below 0 °C, which ensures a large and stable temperature difference across TE modules to produce more electricity. **d** Potential applications in space. The sunny side temperature of the solar panel can reach 120 to 150 °C, while the dark side temperature can drop to −100 to −200 °C. This could create a significant Δ*T* across the TE module, which can enhance the output power and efficiency of PV-TE hybrid systems in space.

process for both the PV and TE modules[63–65], and dynamic matching circuit design for the integrated systems[66] (Supplementary Note 9). The PV-TE hybrid system currently exhibits a significantly higher LCOE than standalone PV and TE modules, but reducing the cost of TE modules and extending annual equivalent operating hours of the hybrid system could make the system a more cost-effective option in the future (Supplementary Note 10). It is also important to note that the disadvantage of its unfavorable LCOE might be tuned down for some special environments (e.g., in aerospace, offshore, or payload-limited environments), where higher power density is prioritized over cost per watt.

In this work, through theoretical analysis and simulation based on a PV-TE Thermo-Electrical Coupling Model, we have found the requirements and conditions for such a PV-TE hybrid system to have maximum efficiency with energy lossless coupling output. Guided by the model above, we predicted that, using the best available PV modules and commercialized TE materials, the maximum efficiency of PV-TE hybrid systems could reach 60.34%. Following these theoretical guidelines, we have fabricated such a hybrid system and achieved the highest efficiency with energy lossless coupling output using solution-processed solar cells (OSCs and PSCs). The optimized OSC-TE hybrid systems achieved high efficiency of 34.85% and 43.16% at 298 K and 313 K under AM 1.5 G solar illumination, respectively. Likewise, the optimized PSC-TE hybrid systems exhibited remarkable efficiency of 42.03% and 50.28% at 298 K and 313 K under AM 1.5 G solar illumination, respectively.

Although the results presented in this work demonstrate great potential for the practical application of PV-TE hybrid systems, further research remains necessary to advance toward real-world applications. These efforts include the use of more advanced solar cells and TE modules to enhance the performance and stability of PV-TE hybrid systems, further studies on large-area fabrication and integration of PV and TE modules, and exploration of system performance under varied application scenarios. These aspects are currently being pursued in our group.

## Methods

### Materials for organic solar cells (OSCs)

Donor polymer PM6 was purchased from Solarmer Materials, Inc. Acceptor molecule L8-BO was provided by Jiaxing Hyper Optoelectronic Technology Co., Ltd. Indium tin oxide (ITO) was purchased from Liaoning Advanced Election Technology. Zinc oxide (ZnO) nanoparticles were synthesized the methods reported in literature[67]. The organic molecule named 2-(3-(dimethylamino)propyl)-1,3-dioxo-2,3-dihydro-1H-benzo[de]-isoquinoline-6,7-dicarboxylic acid (NMA) were synthesized using the methods reported in literature[48].

### Materials for perovskite solar cells (PSCs)

Tin(IV) oxide, 15% in $H_2O$ colloidal dispersion, was provided by Alfa Aesar. $PbI_2$ (99.99%) was purchased from TCI. Cesium iodide (CsI, 99.999%) was purchased from Advanced Election Technology Co., Ltd. 2,2′,7,7′-Tetrakis[N,N-di(4-methoxyphenyl)amino]-9,9′-spiro-bifluorene (Spiro-OMeTAD) was provided by Woerjiming (Beijing) Technical Development Institute. Lithium bis (trifluoromethylsulfonyl)-imide (99.9%) was purchased from Sigma-Aldrich, 4-tertbutylpyridine (96.0%) was purchased from TCI. Poly[bis(4-phenyl)(2,4,6-trimethylphenyl)amine] (PTAA) were all purchased from Xi'an Polymer Light Technology in China. FAI, MACl, and ThPyI were synthesized using the methods reported in literatures[68,69].

### Thermoelectric materials

The micro thermoelectric cells (model 1MD02-024-03, $N = 24$) were purchased from RMT Co., Ltd. Each thermoelectric cell, with dimensions of 2 mm × 2 mm × 0.9 mm, consists of 24 pairs of p-n junctions made from bismuth telluride ($Bi_2Te_3$) material with copper electrodes. The dimensions of a single $Bi_2Te_3$ thermoelectric leg were 0.2 mm × 0.2 mm × 0.3 mm, and the internal resistance and total Seebeck coefficient of each thermoelectric cell were approximately 3.32–3.5 Ω and 10.0 mV/K, respectively. The $Bi_2Te_3$ semiconductor grains used for fabricating large-area flexible thermoelectric devices were sourced from Changsha KunYong New Materials Co., Ltd, with dimensions of 1.0 mm × 1.0 mm × 2.0 mm.

### Device fabrication of OSCs

The OSCs were fabricated following our previous work with an inverted structure of ITO/ZnO/NMA/PM6:L8-BO/$MoO_x$/Ag[48]. Firstly, the indium tin oxide (ITO)-coated glass substrates were cleaned by ultrasonic treatment in detergent, deionized water, acetone, and isopropyl alcohol under ultrasonication for 15 min each and subsequently dried by a nitrogen blow. Subsequently, a 15 nm thick layer of ZnO was deposited by spin-coating a ZnO precursor solution (prepared by dissolving 100 mg zinc acetate dihydrate and 28 μL ethanolamine in 4 mL of 2-methoxyethano) on the top of the ITO glass substrates at 3000 rpm for 40 s. After being baked at 200 °C in the air for 1.0 h, the ZnO-coated substrates were transferred into a nitrogen-filled glove box. For the hybrid ETL of ZnO/NMA, the NMA film was deposited upon ZnO film from its solution with a concentration of 0.4 mg/mL in methyl alcohol with ammonium hydroxide of 2% volume (to ensure good solubility) and then baked on a hot plate at 120 °C for 10 min in ambient atmosphere. For the active layer of PM6:L8-BO (weight ratio of 1:1.2), the PM6:L8-BO blend film was generated by spin-coating the blend solution at a spin-coating rate of 3,000 rpm upon the corresponding ETLs, and then was thermally annealed at 110 °C for 5 min. Then, $MoO_x$ (~2 nm) and Ag (~150 nm) were successively evaporated onto the active layer through a shadow mask. The effective area for the devices was 0.04–0.36 $cm^2$ (step: 0.04 $cm^2$), determined using an optical profilometer.

### Device Fabrication of PSCs

The PSCs were fabricated according to our previous work[49]. The ITO substrate was washed sequentially with distilled water, acetone, and isopropanol. Before use, the ITO was cleaned with ultraviolet ozone for 20 min. The $SnO_2$ electron transport layer (2.5 wt%, diluted by water) was coated on the ITO substrate and annealed in air at 170 °C for 30 minutes. After cooling to room temperature, the substrate was treated with ultraviolet ozone for 10 minutes before spin-coating the perovskite solution. Usually, 1.5 M $PbI_2$ with 2 mol % CsI was dissolved in DMF/DMSO (v/v, 94/6), and then stirred at 70 °C for 4 hours. The $PbI_2$ solution was then deposited by spin coating at 1500 rpm for 30 seconds, dried at 70 °C for 1 minute, and then cooled to room temperature. A solution of 2D spacer (2 mg/mL) in isopropanol (IPA) was spin-coated on the $PbI_2$ film at a spin rate of 2000 rpm for 30 seconds, and annealed at 70 °C for 30 seconds. After cooling to room temperature, a solution of FAI/MACl (90:9 mg $mL^{-1}$) in IPA was spin-coated on top of the $PbI_2$ layer at a rotation speed of 2000 rpm for 35 seconds, followed by thermal annealing at 160 °C for 12 min in the air (relative humidity about 65%). After perovskite formation, the samples were transferred to a nitrogen-filled glove box for further processing. For the passivation layer, the ThPyI solution was dissolved in IPA with 4 mg/mL and spin-coated onto the perovskite surface at a spin rate of 5,000 rpm, without any further processing. Then, spin-coated the Spiro-OMeTAD solution (80 mg of Spiro-OMeTAD, 30 μL of 4-tert-butylpyridine and 35 μL of lithium bis(trifluoromethylsulfonyl)-imide (Li-TFSI, 260 mg/mL in acetonitrile) in 1 mL of chlorobenzene) on the perovskite layer with 6000 rpm for 30 seconds. For the thermal stability of devices, 20 mg PTAA was dissolved in 1 mL toluene, then 10 μL Li-TFSI (260 mg/ml in acetonitrile) and 10 μL 4-tert-butylpyridine were added. The PTAA solution was spin-coated on the surface of the perovskite layer at 2000 rpm for 30 s. Finally, a 12 nm $MoO_3$ layer and 100 nm Ag layer were deposited by thermal evaporation under a pressure of $1.0 \times 10^{-4}$ Pa. The effective area for the devices was 0.04–0.36 $cm^2$ (step: 0.04 $cm^2$), determined using an optical profilometer.

### Fabrication of PV-TE hybrid systems

In the PV-TE hybrid systems, the photovoltaic (PV) solar cells (OSCs and PSCs) parallel module was connected in series with the thermoelectric (TE) module. All TE cell units were connected in series in the TE module. The TE electrodes were soldered with copper wires, while the electrodes of the solar cells were connected to copper wires using conductive silver paste. Subsequently, different electrodes were interconnected via copper wires.

Initially, for optimal thermal energy utilization, a 0.04 $cm^2$ PV-TE hybrid system with a single PV and multiple TE cells was constructed. The PV solar cell and each TE cell have an equal area of 0.04 $cm^2$. In the PV-TE hybrid systems, the TE cells were attached to the bottom of the PV cell using a phase change thermal interface material (PCM). When multiple TE cells were employed, they were added one by one in the stack using the PCM (Supplementary Fig. 7). The PCM (PTM7950 series from Honeywell Co., Ltd.), with a thickness of 0.2 mm and a thermal conductivity of ~8.5 W/mK, can effectively fill interfacial gaps and reduces thermal contact resistance. Polished brass plates (5 mm × 5 mm) were welded to both sides of each TE cell (2 mm × 2 mm × 0.9 mm) to homogenize the temperature distribution and limit adverse thermal radiative losses.

To achieve current matching, parallel modules of OSCs and PSCs with areas ranging from 0.04 to 0.36 $cm^2$ were fabricated (Supplementary Fig. 10). Then multiple TE units were employed in the *xy*-plane to match the effective area of the PV module. For each layer, the total area of the TE cells was equal to the effective area of the PV module. In the *z*-plane, the TE cells were stacked layer by layer using the PCM.

### Fabrication of flexible large-area OSC module

The fabrication of a flexible large-area OSC module was performed following a previously reported procedure[70]. The flexible large-area OSC module was fabricated by applying an inverted architecture of PET/ITO/ZnO/NMA/active layer/MoOx/Ag. ITO-coated PET substrate was ultrasonically treated in detergent, deionized water, acetone, and isopropyl alcohol in sequence for 15 min, followed by blowing dry using argon gas. Afterward, the ZnO layer was blade-coated on the pre-cleaned ITO-coated glass at 50 °C in air with a coating velocity of 10 mm/s and a blade-substrate gap of 200 μm, followed by annealing at 120 °C for 15 mins in atmospheric air. After that, a thin film of NMA was blade-coated on ZnO in the air with a coating velocity of 10 mm/s and a blade-substrate gap of 150 μm. PM6: BTP-BO-4Cl (1:1.2, D: 9 mg/mL) in chlorobenzene with 0.3 vol% 1,8-diiodooctane (DIO) was blade-coated at 60 °C with a coating velocity of

20 mm/s and a blade-substrate gap of 400 μm in air. Finally, MoOx (~6 nm) and Ag (~150 nm) were successively evaporated onto the active layer through a shadow mask ($2 \times 10^{-4}$ Pa). The schematics of the large-area module consisting of four sub-cells connected in series using the methods reported in literature[71]. The photograph of the flexible large-area OSC module with a 14.4 $cm^2$ effective area is shown in Supplementary Fig. 22.

### Fabrication of flexible thermoelectric module

The dimensions of the p-type and n-type thermoelectric legs based on bismuth telluride materials are 1.0 mm × 1.0 mm × 2.0 mm. An array comprising multiple p-n junction pairs, thermally in parallel and electrically in series, was fabricated with dimensions of 55 mm × 55 mm. Copper wires were used as electrodes to connect different legs. The assembled thermoelectric array was then cast using PDMS, which was prepared by mixing PDMS precursor with curing agent at a mass ratio of 10:1. The embedded array was subsequently cured in an oven at 80 °C for 4 h. Finally, a 1.5 mm-thick PDMS composite layer, containing BN and $Al_2O_3$ to enhance thermal conductivity, was cast and cured on both sides of the thermoelectric array (Supplementary Fig. 23).

### Fabrication of PDMS/BN/$Al_2O_3$/DM fabrics

The PDMS/BN/$Al_2O_3$/DM fabrics were prepared using a 3D extrusion process and a woven process (Supplementary Fig. 24a, b). Initially, the PDMS precursor and curing agent were mixed at a mass ratio of 10:1. Subsequently, BN (500 nm), $Al_2O_3$ (50 nm), and DM (n-Docosane microcapsule) were incorporated into the PDMS mixture in a container. Then, the mixture was placed in a vacuum mixer for 5 minutes at room temperature to achieve a homogeneous phase. The resulting PDMS/BN/$Al_2O_3$/DM mixture was transferred to a syringe, extruded, and subsequently cured at 80 °C for 4 h. The fabricated composite fibers had a diameter of 0.6 mm. Finally, the fibers were woven into a fabric, which was integrated into clothing for cooling and heat dissipation applications in flexible PV-TE hybrid devices.

### Measurement of *J-V* curves

The current density-voltage (*J-V*) characteristics of PV-TE hybrid systems were obtained using a Keithley 2400 source measure unit, the scan speed and dwell times of the *J-V* curves were fixed at 0.02 V $s^{-1}$ and 20 ms, respectively. The photocurrent was measured under AM 1.5 G illumination using an SS-X50 solar simulator, calibrated with a standard Si solar cell (Enli Technology CO., Ltd., Taiwan, and calibrated report can be traced to NREL).

### Measurement of thermoelectric signals

The thermoelectric signals were obtained using a Keithley 2400 source measure unit. Temperature variation and distribution in this work were recorded through a thermocouple, and the temperature can be read out in real-time.

### Measurement of photostability and thermal cycling stability

The photostability testing was conducted following the ISOS-L-1 protocol. The standalone PV (OSC and PSC) and the PV-TE hybrid system (OSC-TE and PSC-TE) were encapsulated and tested under continuous 1-sun LED illumination at the open-circuit state in ambient air (20–30 °C, 40–60% RH). The LED spectrum is shown in Supplementary Fig. 16c. *J-V* characteristics were recorded using a solar simulator after each 48 h light-soaking period.

The thermal cycling stability testing was conducted following the ISOS-T-2 protocol. The standalone PV (OSC and PSC) and the PV-TE hybrid system (OSC-TE and PSC-TE) were encapsulated, then placed in an oven and thermally cycled between 25 °C and 65 °C under dark, open-circuit conditions. *J-V* characteristics were recorded using a solar simulator after every 20 thermal cycling periods.

### Reporting summary

Further information on research design is available in the Nature Portfolio Reporting Summary linked to this article.

## Data availability

All data are available in the main text or the Supplementary Materials. Additional information can be obtained from corresponding authors upon request. Source data are provided with this paper.

## References


1. Li, S., Li, Z., Wan, X. & Chen, Y. Recent progress in flexible organic solar cells. *eScience* **3**, 100085 (2023).
2. Li, C. et al. Organic solar cells with 21% efficiency enabled by a hybrid interfacial layer with dual-component synergy. *Nat. Mater.* **24**, 1626–1634 (2025).
3. Wang, C. et al. Enhancing performance of tin-based perovskite solar cells via fused-ring electron acceptor. *eScience* **3**, 100113 (2023).
4. Liu, C. et al. Two-dimensional perovskitoids enhance stability in perovskite solar cells. *Nature* **633**, 359–364 (2024).
5. Omair, Z. et al. Ultraefficient thermophotovoltaic power conversion by band-edge spectral filtering. *Proc. Natl. Acad. Sci.* **116**, 15356–15361 (2019).
6. Fan, D. et al. Near-perfect photon utilization in an air-bridge thermophotovoltaic cell. *Nature* **586**, 237–241 (2020).
7. Wang, Z. et al. Lightweight, passive radiative cooling to enhance concentrating photovoltaics. *Joule* **4**, 2702–2717 (2020).
8. Apostoleris, H., Stefancich, M. & Chiesa, M. Tracking-integrated systems for concentrating photovoltaics. *Nat. Energy* **1**, 16018 (2016).
9. Guo, J. & Huai, X. Maximizing electric power through spectral-splitting photovoltaic-thermoelectric hybrid system integrated with radiative cooling. *Adv. Sci.* **10**, 2206575 (2023).
10. LaPotin, A. et al. Thermophotovoltaic efficiency of 40%. *Nature* **604**, 287–291 (2022).
11. Rezania, A. & Rosendahl, L. A. Feasibility and parametric evaluation of hybrid concentrated photovoltaic-thermoelectric system. *Appl. Energy* **187**, 380–389 (2017).
12. Meng, L. et al. Organic and solution-processed tandem solar cells with 17.3% efficiency. *Science* **361**, 1094–1098 (2018).
13. Sun, Y. et al. Flexible organic photovoltaics based on water-processed silver nanowire electrodes. *Nat. Electron.* **2**, 513–520 (2019).
14. Zhu, L. et al. Achieving 20.8% organic solar cells via additive-assisted layer-by-layer fabrication with bulk p-i-n structure and improved optical management. *Joule* **8**, 1–16 (2024).
15. Fu, J. et al. Two-step crystallization modulated through acenaphthene enabling 21% binary organic solar cells and 83.2% fill factor. *Nat. Energy* **10**, 1251–1261 (2025).
16. Liu, S. et al. Buried interface molecular hybrid for inverted perovskite solar cells. *Nature* **632**, 536–542 (2024).
17. Li, S. et al. High-efficiency and thermally stable $FACsPbI_3$ perovskite photovoltaics. *Nature* **635**, 82–88 (2024).
18. Green, M. A. et al. Solar cell efficiency tables (Version 64). *Prog. Photovolt. Res. Appl.* **32**, 425–441 (2024).
19. Xu, L. et al. Parasitic heating of perovskite- and silicon-based photovoltaics. *Adv. Energy Mater.* **13**, 2300013 (2023).
20. Xu, L. et al. Heat generation and mitigation in silicon solar cells and modules. *Joule* **5**, 631–645 (2021).
21. Liu, Z. et al. Novel integration of carbon counter electrode based perovskite solar cell with thermoelectric generator for efficient solar energy conversion. *Nano Energy* **38**, 457–466 (2017).
22. Xu, L. et al. Efficient perovskite photovoltaic-thermoelectric hybrid device. *Adv. Energy Mater.* **8**, 1702937 (2018).

23. Wang, N., Han, L., He, H., Park, N.-H. & Koumoto, K. A novel high-performance photovoltaic-thermoelectric hybrid device. *Energy Environ. Sci.* **4**, 3676–3679 (2011).
24. Liu, W., Sun, S. & Zhu, X. Organic photovoltaics integrated with thermoelectric generator achieving low critical temperature difference and efficient energy conversion. *Adv. Funct. Mater.* **32**, 2109410 (2022).
25. Zhao, P. et al. Plasticity in single-crystalline $Mg_3Bi_2$ thermoelectric material. *Nature* **631**, 777–782 (2024).
26. Wang, D. et al. Multi-heterojunctioned plastics with high thermoelectric figure of merit. *Nature* **632**, 528–535 (2024).
27. Yang, Q. et al. Flexible thermoelectrics based on ductile semiconductors. *Science* **377**, 854–858 (2022).
28. Karthikeyan, V. et al. Three dimensional architected thermoelectric devices with high toughness and power conversion efficiency. *Nat. Commun.* **14**, 2069 (2023).
29. Lee, B. et al. High-performance compliant thermoelectric generators with magnetically self-assembled soft heat conductors for self-powered wearable electronics. *Nat. Commun.* **11**, 5948 (2020).
30. Wolf, M. Performance analyses of combined heating and photovoltaic power systems for residences. *Energy Conver* **16**, 79–90 (1976).
31. Zhang, Y. et al. Integrated energy-harvesting system by combining the advantages of polymer solar cells and thermoelectric devices. *J. Phys. Chem. C.* **117**, 24685–24691 (2013).
32. Zhou, Y. et al. A highly-efficient concentrated perovskite solar cell-thermoelectric generator tandem system. *J. Energy Chem.* **59**, 730–735 (2021).
33. Zhu, W., Deng, Y., Wang, Y., Shen, S. & Gulfam, R. High-performance photovoltaic-thermoelectric hybrid power generation system with optimized thermal management. *Energy* **100**, 91–101 (2016).
34. Vorobiev, Y., González-Hernández, J., Vorobiev, P. & Bulat, L. Thermal-photovoltaic solar hybrid system for efficient solar energy conversion. *Sol. Energy* **80**, 170–176 (2006).
35. Zhou, Y. et al. Perovskite solar cell-thermoelectric tandem system with a high efficiency of over 23%. *Mater. Today Energy* **12**, 363–370 (2019).
36. Wang, J., Li, Y., Yang, B. & Jiang, L. Multi-optimized reconfiguration of hybrid photovoltaic-thermoelectric generation (PV-TEG) system for performance enhancement. *Energy Convers. Manag.* **307**, 118373 (2024).
37. Rezania, A., Sera, D. & Rosendahl, L. A. Coupled thermal model of photovoltaic-thermoelectric hybrid panel for sample cities in Europe. *Renew. Energy* **99**, 127–135 (2016).
38. Deng, Y., Zhu, W., Wang, Y. & Shi, Y. Enhanced performance of solar-driven photovoltaic-thermoelectric hybrid system in an integrated design. *Sol. Energy* **88**, 182–191 (2013).
39. Yin, E. & Li, Q. Achieving extensive lossless coupling of photovoltaic and thermoelectric devices through parallel connection. *Renew. Energy* **193**, 565–575 (2022).
40. Park, K.-T. et al. Lossless hybridization between photovoltaic and thermoelectric devices. *Sci. Rep.* **3**, 2123 (2013).
41. Servaites, J. D., Yeganeh, S., Marks, T. J. & Ratner, M. A. Efficiency enhancement in organic photovoltaic cells: consequences of optimizing series resistance. *Adv. Funct. Mater.* **20**, 97–104 (2010).
42. Lorenzi, B., Acciarri, M. & Narducci, D. Suitability of electrical coupling in solar cell thermoelectric hybridization. *Designs* **2**, 32 (2018).
43. Lin, J., Liao, T. & Lin, B. Performance analysis and load matching of a photovoltaic-thermoelectric hybrid system. *Energy Convers. Manag.* **105**, 891–899 (2015).
44. Jin, Q. et al. Flexible layer-structured $Bi_2Te_3$ thermoelectric on a carbon nanotube scaffold. *Nat. Mater.* **18**, 62–68 (2019).
45. Wan, C. et al. Flexible n-type thermoelectric materials by organic intercalation of layered transition metal dichalcogenide $TiS_2$. *Nat. Mater.* **14**, 622–627 (2015).
46. Hao, F. et al. High efficiency $Bi_2Te_3$-based materials and devices for thermoelectric power generation between 100 and 300 °C. *Energy. Environ. Sci.* **9**, 3120–3127 (2016).
47. Ahmad, A. et al. Largely enhanced thermoelectric performance in p-type $Bi_2Te_3$-based materials through entropy engineering. *Energy Environ. Sci.* **17**, 695–703 (2024).
48. Li, S. et al. Achieving over 18% efficiency organic solar cell enabled by a ZnO-based hybrid electron transport layer with an operational lifetime up to 5 years. *Angew. Chem. Int. Ed.* **61**, e202207397 (2022).
49. Gao, Y. et al. Controlled nucleation and oriented crystallization of methylammonium-free perovskites via in situ generated 2D perovskite phases. *Adv. Mater.* **36**, e2405921 (2024).
50. Basu, R. et al. Large-area organic photovoltaic modules with 14.5% certified world record efficiency. *Joule* **8**, 970–978 (2024).
51. Liang, Y. et al. A matrix-confined molecular layer for perovskite photovoltaic modules. *Nature* **648**, 91–96 (2025).
52. He, J. et al. Advances in the applications of thermoelectric generators. *Appl. Therm. Eng.* **236**, 121813 (2024).
53. Liu, B. et al. Inverted organic solar cells with an in situ-derived $SiO_xN_y$ passivation layer and power conversion efficiency exceeding 18%. *Nat. Photon.* **19**, 195–203 (2025).
54. Lin, Y. et al. A $Nd@C_{82}$-polymer interface for efficient and stable perovskite solar cells. *Nature* **642**, 78–84 (2025).
55. Qin, J. et al. Improved damp heat and thermal cycling stability of organic solar cells. *Nat. Energy* **10**, 1439–1449 (2025).
56. Li, G. et al. Stabilizing high-efficiency perovskite solar cells via strategic interfacial contact engineering. *Nat. Photon.* **20**, 55–62 (2025).
57. Palaporn, D. et al. Thermoelectric materials for space explorations. *Mater. Adv.* **5**, 5351–5364 (2024).
58. Fu, P. et al. Integrating large-area perovskite solar module with thermoelectric generator for enhanced and stable power output. *Nano Energy* **65**, 104009 (2019).
59. He, Z., Yang, M., Wang, L., Bao, E. & Zhang, H. Concentrated photovoltaic thermoelectric hybrid system: an experimental and machine learning study. *Engineered Sci.* **15**, 47–56 (2021).
60. Kim, Y. J. et al. High-performance monolithic photovoltaic-thermoelectric hybrid power generator using an exothermic reactive interlayer. *ACS Appl. Energy Mater.* **2**, 2381–2386 (2019).
61. Ma, R. et al. Organic solar cells: beyond 20%. *Sci. China Mater.* **68**, 1689–1701 (2025).
62. Liu, D. et al. Lattice plainification advances highly effective SnSe crystalline thermoelectrics. *Science* **380**, 841–846 (2023).
63. Yang, F., Huang, Y., Li, Y. & Li, Y. Large-area flexible organic solar cells. *npj Flex. Electron.* **5**, 30 (2021).
64. Yang, C. et al. Achievements, challenges, and future prospects for industrialization of perovskite solar cells. *Light Sci. Appl.* **13**, 227 (2024).
65. Wong, W. P. et al. Bismuth telluride-based thermoelectric generators: Advances in synthesis, performance enhancement, and device applications. *J. Power Sources* **653**, 237722 (2025).
66. Fang, X. & Yang, Q. Dynamic reconfiguration of photovoltaic array for minimizing mismatch loss. *Renew. Sust. Energy Rev.* **191**, 114160 (2024).
67. Beek, W. J. E., Wienk, M. M. & Janssen, R. A. J. Hybrid polymer solar cells based on zinc oxide. *J. Mater. Chem.* **15**, 2985–2988 (2005).
68. Lee, M. M., Teuscher, J., Miyasaka, T., Murakami, T. N. & Snaith, H. J. Efficient hybrid solar cells based on meso-superstructured organometal halide perovskites. *Science* **338**, 643–647 (2012).
69. Xu, Z. et al. Phase distribution and carrier dynamics in multiple-ring aromatic spacer-based two-dimensional Ruddlesden-Popper perovskite solar cells. *ACS Nano* **14**, 4871–4881 (2020).

70. Wang, Z. et al. Self-sustaining personal all-day thermoregulatory clothing using only sunlight. *Science* **382**, 1291–1296 (2023).
71. Zhang, S. et al. A large area organic solar module with non-halogen solvent treatment, high efficiency, and decent stability. *Sol. RRL* **7**, 2300029 (2023).

## Acknowledgements

This work is supported by the National Key R&D Program of China (2022YFB4200400) (Y.C.) and the National Natural Science Foundation of China (Grant No. 52025033, 52273248, 52303238, and 52473215) (Y.C., R.M., and D.Z.).

## Author contributions

Z.Y. and D.Z. contributed equally to this work. Y.C. and R.M. conceived and designed the project. Z.Y., D.Z., L.L., and Y.G. performed the device fabrication. Z.Y. and D.Z. carried out the performance measurements and simulation calculations. Y.C., R.M., Z.Y., D.Z., Y.L., and X.W. analyzed all experimental and simulated data. Z.Y. and D.Z. prepared the manuscript under the supervision of Y.C. and R.M. All the authors contributed to the revision and comments to the manuscript.

## Competing interests

The authors declare no competing interests.

## Additional information

**Supplementary information** The online version contains supplementary material available at https://doi.org/10.1038/s41467-026-71389-w.

**Correspondence** and requests for materials should be addressed to Rujun Ma or Yongsheng Chen.

**Peer review information** *Nature Communications* thanks Lin Jiang, and the other, anonymous, reviewer(s) for their contribution to the peer review of this work. A peer review file is available.